Conformational Backbone Dynamics of the Cyclic Decapeptide Antamanide. Application of a New Multiconformational Search Algorithm Based on NMR Data†

M. J. Blackledge,‡ R. Brüschweiler,§ C. Griesinger,‖ J. M. Schmidt,⊥ Ping Xu, and R. R. Ernst*

Laboratorium für Physikalische Chemie, Eidgenössische Technische Hochschule, 8092 Zürich, Switzerland

Received April 26, 1993; Revised Manuscript Received July 27, 1993•

ABSTRACT: A general procedure for the analysis of biomolecular structures by NMR in the presence of rapid conformational dynamics has been applied to the study of the cyclic decapeptide antamanide. Two-dimensional experiments, relaxation measurements in the rotating frame, and homo- and heteronuclear coupling constant determinations have been used to characterize the dynamic properties of the molecule, in combination with a novel search algorithm for investigating multiconformational equilibria. Direct evidence for the presence of a conformational exchange process with an activation energy of ~20 kJ mol^{-1} and an exchange lifetime of ~25 μs at 320 K has been obtained from rotating frame relaxation measurements. This evidence is combined with the information derived from the multiconformational search algorithm MEDUSA to propose sets of structures that coexist in a dynamic exchange equilibrium.

The development of two-dimensional (2D)[1] NMR techniques for spectral assignment and dipolar cross-relaxation measurement (Wüthrich, 1986; Ernst et al., 1987) has led, in conjunction with the emergence of computer-assisted molecular modeling techniques, to powerful procedures for the determination of the structure of peptides and medium-sized proteins in solution. The use of either distance geometry (Crippen, 1981; Havel & Wüthrich, 1984; Braun and Gō, 1985; Crippen and Havel, 1988) or restrained molecular dynamics (rMD) calculations (Kaptein et al., 1985; de Vlieg et al., 1986), in combination with internuclear distance and backbone dihedral angle constraints derived from NMR measurements, has been shown to generate viable molecular solution structures (Wagner et al., 1984; Clore et al., 1985; Kline et al., 1988).

The simplest model, used to convert cross-relaxation and scalar coupling constant measurements into distance and angular constraints and subsequently into a proposed three-dimensional molecular structure, assumes the existence of a single rigid conformation. In the case of rapid exchange between two or more significantly populated conformers, the NMR data are more likely to reflect a population-weighted average. Misinterpretation of such data in terms of a static structure would result in false conclusions. The presence of more than one conformation contributing to the NMR signal can sometimes, but not always, be inferred from inconsistencies among the NMR data in terms of a rigid structure. The consideration of intramolecular dynamics will become increasingly important in the context of structural studies when NMR cross-relaxation measurements are interpreted more quantitatively, looking for subtle structural effects.

The study of the conformational dynamics of biomolecules is also important for its own sake. The interaction between larger molecules almost invariably requires a certain molecular flexibility to allow the formation of tightly bound associates. For example, active sites in a pocket of an enzyme can often be approached only by way of a temporal opening of the pocket. When a molecule coexists in several conformations, only one of them may be responsible for its enzymatic or functional activity, and conformational rearrangements must take place on a sufficiently short time scale for high activity.

In numerous structure investigations by NMR, dynamic effects have been taken into account. We would like to mention just a few examples. From a study of the acyl carrier protein, it was inferred that the presence of two exchanging conformations gives rise to an average set of NMR data (Kim & Prestegard, 1989). In this case, conformations, obtained from a number of rMD calculations, were combined in pairs, and a fit of the computed average distance constraints to the experimental data led to the optimum population ratio. The structural coordinates of the conformations were then optimized for a fixed population ratio in an attempt to improve the fit. The agreement based on two structures turned out to be significantly better than by assuming a single rigid conformation. The authors nevertheless retain a cautious perspective by suggesting that an improvement in the quality

† This research was supported by a Royal Society Fellowship to M.J.B. and by the Swiss National Science Foundation. J.M.S. acknowledges a postdoctoral grant from the Deutsche Forschungsgemeinschaft.

‡ Present address: Institut de Biologie Structurale, 41, Avenue des Martyrs, 38027 Grenoble, France.

§ Present address: The Scripps Research Institute, Department of Molecular Biology, 10666 N. Torrey Pines Rd., La Jolla, CA 92037.

‖ Present address: J. W. Goethe Universität, Institut für Organische Chemie, Marie-Curie-Str. 11, D-60439 Frankfurt, Germany.

⊥ Present address: Institut für Biophysikalische Chemie, Universitätsklinikum, Haus 75A, Theodor-Stern-Kai 7, D-60590 Frankfurt, Germany.

• Abstract published in *Advance ACS Abstracts,* September 15, 1993.

[1] Abbreviations: ABNR, adapted-base Newton–Raphson algorithm; ADC, absent distance constraint; CHARMM, a molecular dynamics simulation program; COLOC, a sequence for heteronuclear long-range correlation; COSY, 2D correlation spectroscopy; DANTE, a frequency-selective pulse sequence; DC, distance constraint; E.COSY, 2D exclusive correlation spectroscopy; HMBC, heteronuclear multiple-bond correlation; HMQC, heteronuclear multiple-quantum correlation; HSQC, heteronuclear single-quantum correlation; MEDUSA, multiconformational evaluation of distance information using a stochastically constrained minimization algorithm; MLEV-17, a multiple-pulse decoupling sequence; NMR, nuclear magnetic resonance; NOE, nuclear Overhauser effect; NOESY, 2D nuclear Overhauser effect spectroscopy; rf, radio frequency; rMD, restrained molecular dynamics; TOCSY, 2D total correlation spectroscopy; ROESY, 2D rotating frame Overhauser effect spectroscopy; WEFT, water-eliminated Fourier transform spectroscopy; 2D, two-dimensional; 2QF-COSY, double-quantum-filtered correlation spectroscopy.

0006-2960/93/0432-10960$04.00/0

of a fit by introducing an additional degree of freedom should not be overinterpreted as proof of a multiconformational equilibrium.

An investigation of a cyclic somatostatin analogue has also exhibited NOESY-derived distances that were in contradiction to the rigid structures produced by rMD calculations (Pepermans et al., 1988). It led to the suggestion of a dynamic equilibrium of four structures. The authors discuss the limitations of incomplete sampling of the conformational space and the bias thus incurred in the selection of structures.

The rate constants of intramolecular dynamic processes can be determined by relaxation measurements in the laboratory or the rotating frame. These investigations are most sensitive to conformational dynamics when the rate constant is comparable either to the Larmor frequency, ω_0, to $2\omega_0$, or to the radio frequency (rf) field strength, $\omega_1 = -\gamma B_1$. Measurements in the rotating frame are particularly convenient because the sensitive frequency window can be adjusted by selecting the rf field strength, B_1 (Deverell et al., 1970; Bleich & Glasel, 1978). Several examples of motional processes in peptides have been investigated in this manner (Kopple et al., 1986, 1988).

In many previous accounts of dynamic effects in biomolecular structure determination, the procedure of analysis starts with structures that were derived on the assumption of a single conformation. Such structures are then combined in pairs, triples, or multiples in an attempt (that hardly can fail) to improve the fit of the experimental data. The initial assumption of a single conformation, however, limits the accessible structures, as each structure is produced from an analysis designed to minimize the deviations from *all* measured structural constraints.

In this paper, an improved structural search protocol shall be combined with rotating frame relaxation measurements to explore the conformational dynamics of the cyclic decapeptide antamanide (-^{1}Val-^{2}Pro-^{3}Pro-^{4}Ala-^{5}Phe-^{6}Phe-^{7}Pro-^{8}Pro-^{9}Phe-^{10}Phe-) (I). Antamanide has biological activity as an antidote

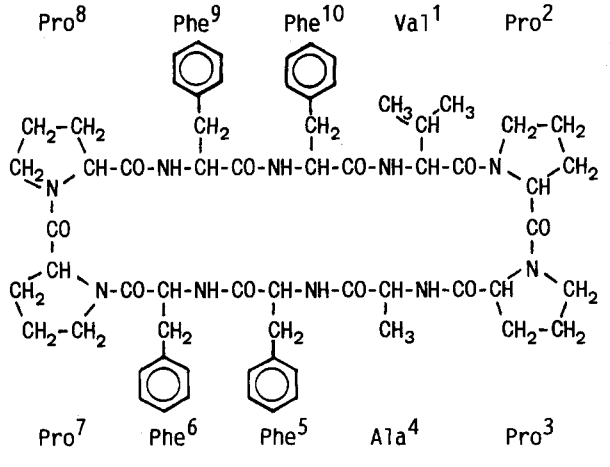

(I)

against the poisonous phalloidins that occur in the mushroom *Amanita phalloides* (Wieland & Faulstich, 1978). Remarkably, antamanide is contained in small quantities in the same mushroom. In mammals, phalloidins block the depolymerization of F-actin into G-actin in the liver cell membrane. This process can be prevented by the presence of antamanide (Faulstich et al., 1974).

It has been suggested, initially from 1D NMR measurements (Patel, 1973) and subsequently from ultrasonic absorption measurements (Burgermeister et al., 1974), that antamanide exists in solution in an equilibrium of rapidly interchanging conformers ($k \sim 10^6$ s^{-1}). In a more recent analysis based on NMR investigations of antamanide in chloroform, inconsistencies between structurally dependent NMR parameters and a single stable conformation were cited as further evidence for the presence of more than one significantly populated conformer in solution (Kessler et al., 1989b). In the latter investigation, the authors proposed a dynamic equilibrium between two or four conformations involving the X-ray structure (Karle et al., 1979) and a conformation resulting from an rMD calculation using NOESY-derived distance constraints. These two conformations separately disagree with the available NMR evidence, but could, in combination, be shown to satisfy the data.

The novel search algorithm, termed MEDUSA (*M*ulti-conformational *E*valuation of *D*istance information *U*sing a *S*tochastically constrained minimization *A*lgorithm) (Brüschweiler et al., 1991), that will be applied in the present work, has been developed for the systematic investigation of multiple conformations in rapid exchange in solution based on structural constraints from NMR measurements. Conformers partially fulfilling the NMR distance constraints are produced by an energy-minimization procedure with the sequential application of pseudoenergy potentials for each of the constrained internuclear distances. Only those constraints which, in combination, generate energetically viable structures are retained; the molecule is thus "shaped" into a form satisfying a subset of the distance constraints while remaining energetically realistic. The resulting conformations are then combined in dynamic exchange systems to fulfill simultaneously all experimental constraints.

MATERIALS AND METHODS

The conformational analysis procedure consists of the following steps: The backbone proton magnetic resonances are assigned using standard COSY and NOESY spectra. A series of cross-relaxation experiments is performed to produce a set of internuclear distance constraints (termed DCs in this paper) between backbone protons and a set of absent distance constraints (termed ADCs) emanating from the absence of cross peaks between backbone protons. Homo- and heteronuclear correlation experiments are performed to measure ^3J coupling constants, which are used to determine limits on the backbone dihedral angles, ϕ. In addition, the hydrogen bond dynamics is analyzed by proton $T_{1\rho}$ measurements. The MEDUSA procedure (Brüschweiler et al., 1991) is then applied to determine an extensive set of low-energy conformations that partially fulfill the distance constraints. All pairs of structures from the ensemble are then investigated regarding their ability to satisfy together all experimental constraints. The relative populations within these pairs are optimized to satisfy the experimentally determined structural constraints. The ensemble of conformational pairs with acceptable fitting properties is then further restrained, taking into account also the derived hydrogen bond dynamics.

Two antamanide samples were obtained as gifts from Prof. Horst Kessler, Technische Universität München, and from Hoechst AG, Frankfurt (Dr. H. Kogler). Another sample was purchased from Orpegen GmbH, Heidelberg, Germany. Antamanide was used without further purification as a 40 mM solution in 99.98% chloroform-*d* (5-mm tube) and a 12.4 mM solution in 99.98% chloroform-*d* (10-mm tube). It should be noted that the water content of the crystalline antamanide was not controlled. It can therefore not be excluded that the samples may contain a tiny amount of water that could form a partial hydrate of antamanide.

A uniformly ^{13}C-enriched sample of antamanide was used for measuring ^{13}C–^{1}H J-coupling constants. It was synthesized

by Prof. Saburo Aimoto, Institute of Protein Research, Osaka University, using the solid-phase method and cyclization in the presence of *p*-nitrophenol and 1-[3-(dimethylamino)-propyl]-3-ethylcarbodiimide hydrochloride. The ^{13}C-labeled amino acids were supplied by Prof. Masatsune Kainosho, Department of Chemistry, Tokyo Metropolitan University.

NMR Methods. (A) Cross-Relaxation Measurements. Two-dimensional spectra were recorded on Bruker MSL-400, AM-500, and AMX-600 spectrometers operating at 400.13-, 500.13-, and 600.13-MHz proton resonance frequencies, respectively.

The assignment of the ^1H NMR spectra of antamanide at temperatures of 250, 303, and 320 K was achieved by standard phase-sensitive 2QF-COSY spectra (Piantini et al., 1982) and NOESY spectra (Jeener et al., 1979; Kumar et al., 1981). The 2QF COSY data were collected with 512 t_1 increments and 8192 data points in t_2, yielding, after zero-filling, a 1024 × 8192 data matrix. The NOESY data were recorded with 700 increments in the t_1 dimension and 4096 data points in t_2, again Fourier-transformed with zero-filling to a 1024 × 8192 data matrix. The spectra were recorded with a spectral width of 3350 Hz. TPPI was used to distinguish positive and negative frequencies (Marion & Wüthrich, 1983). Chemical shifts are referenced relative to the proton resonance of the undeuterated fraction of $CHCl_3$ at δ = 7.24 ppm and to the ^{13}C resonance of $CDCl_3$ at 77.7 ppm (shifts from TMS).

The cross peaks, required for the backbone resonance assignment, were well resolved except for the overlap of some NH and aromatic resonances at certain temperatures. The overlap problem was resolved by noting that the ring protons of phenylalanine have a longer longitudinal relaxation time than the NH protons (approximately a factor of 4 at any given temperature). This suggested the use of a T_1-weighted WEFT-like experiment (Patt & Sykes, 1972) in which the normal NOESY pulse sequence is preceded by a nonselective inversion pulse followed by a delay which is adjusted to the zero-crossing of the longitudinal magnetization from the slower relaxing aromatic resonances, while at the same time the NH nuclei with the shorter T_1 are allowed to essentially fully relax.

A single set of NMR signals was observed at all temperatures, implying the existence of either a single rigid conformation or a dynamic equilibrium of conformers interconverting rapidly on the NMR time scale. The assignment of the antamanide spectra agreed with data available from previous studies in $CDCl_3$ under comparable conditions (Müller, 1986; Kessler et al., 1989a).

The NOESY spectra were measured at three mixing times (100, 150, and 250 ms) in order to test for the linearity of the cross-relaxation buildup. Figure 1 shows an excerpt from the 500-MHz NOESY spectrum for a mixing time of 150 ms. To further check for possible spin-diffusion effects, a ROESY experiment (700 t_1 increments and 4000 data points in t_2; mixing time τ_m = 150 ms; rf field strength = 2 kHz) (Bothner-By et al., 1984) was performed at 250 K and compared with NOESY data collected under identical conditions. In the slow-motional or low-temperature regime, where NOESY cross peaks are positive with respect to the diagonal while ROESY cross peaks remain negative, the effects of spin diffusion on the distances derived with the two methods should be opposite in sign (Neuhaus & Williamson, 1989). The consistency in the distances obtained from NOESY and ROESY spectra indicate negligible spin-diffusion effects.

The NOE cross-peak analysis was based on the initial rate approximation according to a two-spin model. To determine internuclear distances, cross-peak volumes, $V_{i,j}$, were compared with the average volume, $V_{geminal}$, of two geminal cross peaks,

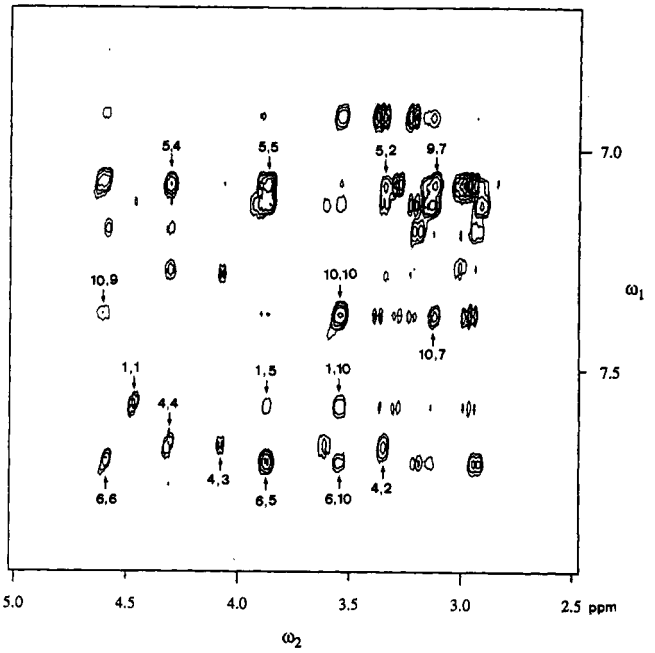

FIGURE 1: NH/H_α region from a 500-MHz NOESY spectrum of antamanide in chloroform for a mixing time of 150 ms at 250 K. Interresidue NH–H_α cross peaks, relevant for distance constraints, are indicated by the ordered pairs of numbers of the respective amino acid residues. The region also contains cross peaks to aromatic protons.

$^3Pro_{\beta\beta}$ and $^8Pro_{\gamma\gamma}$, with known internuclear distance $r_{geminal}$. ^3Pro and ^8Pro are known to lack significant internal mobility and exhibit the relaxation properties of a rigid tumbling molecule (Mádi et al., 1990). The distance $r_{i,j}$ was deduced by the relation $r_{i,j} = (V_{geminal}/V_{i,j})^{1/6} r_{geminal}$ (Noggle & Schirmer, 1971). The distances $r_{i,j}$ are strictly meaningful only in the absence of motion. In the case of a flexible molecule, they have to be regarded as motional averages and serve as a basis for the determination of interchanging conformations as described below.

Exclusively backbone–backbone interactions have been used for the subsequent structure determination to avoid the influence of side-chain motions that would additionally complicate the conformational analysis. From NOESY and ROESY spectra recorded at 250 K with a mixing time of 150 ms, 23 backbone–backbone distance constraints (DCs), listed in Table I, have been determined. The statistical error in the deduced distances is estimated to be smaller than 0.1 Å. In addition, an analysis of missing cross peaks was performed, leading to a list of backbone–backbone absent DCs (abbreviated ADCs). In the terminology of distance geometry, an ADC corresponds to a proton pair with a lower distance bound which exceeds the sum of the involved van der Waals radii. No upper bound is implied. In the following, the absence of a cross peak is attributed to a minimum distance of 3.7 Å between the involved nuclei. Table I contains 82 such absent distance constraints. Lack of spectral resolution led us to reject the intra- and interresidual cross peaks ^9Phe NH–^9Phe H_α and ^9Phe NH–^8Pro H_α, which appeared in the data set of Kessler et al. (1988). Comparing the data set of Table I with the one given by Kessler et al. (1988), we note that in six cases the distances of Kessler et al. are shorter by 0.1–0.2 Å, in two cases by 0.3 Å, and in one case by 0.4 Å. In five cases the distances are the same, and in one case the distance given by Kessler et al. is longer. It is interesting to note that in all of the latter six cases the distance is less than or equal to 2.5 Å, whereas in the first nine cases the distance is always greater than 2.6 Å. This shows that the discrepancies occur pre

Table I: Backbone Distance Constraints for Antamanide Derived from a NOESY Spectrum Measured at 250 K[a]

	1N	4N	5N	6N	9N	10N	1α	2α	3α	4α	5α	6α	7α	8α	9α	10α
1N		A	X	A	A	3.1	2.9	A	A	A	3.3	A	A	A	A	3.0
4N	A		3.0	A	A	A	A	2.8	3.3	2.9	A	A	A	A	A	A
5N	X	141		3.0	A	A	A	2.9	X	2.4	2.3	A	X	A	A	X
6N	A	A	138		A	3.1	A	A	A	A	2.6	2.9	A	A	A	3.1
9N	A	A	A	A		X	A	A	A	X	X	X	2.5	X	X	A
10N	117	A	A	122	X		A	A	A	A	X	X	2.9	A	3.1	2.2
1α	170	A	A	A	A	A		A	A	A	A	A	A	A	A	A
2α	A	208	163	A	A	A	A		2.1	X	X	A	A	A	A	A
3α	A	77	X	A	A	A	A	1209		A	A	A	X	A	A	A
4α	A	173	529	A	X	A	A	X	A		A	A	A	A	A	A
5α	79	A	685	321	X	X	A	X	A	A		A	A	A	A	2.5
6α	A	A	A	169	X	X	A	A	A	A	A		A	A	A	A
7α	A	A	X	A	411	168	A	A	X	A	A	A		2.1	A	A
8α	A	A	A	A	X	A	A	A	A	A	A	A	1165		A	A
9α	A	A	A	A	X	113	A	A	A	A	A	A	A	A		A
10α	137	A	X	113	A	881	A	A	A	A	405	A	A	A	A	

[a] Upper right: distance constraints, $r_{i,k}$, in Å; lower left: cross-peak volumes normalized such that a volume $V = 3000$ corresponds to an internuclear distance of 1.795 Å. Absent cross peaks (A) are defined by $V < 40$ and $r_{i,k} > 3.7$ Å; X signifies unresolved NOE cross peaks.

dominantly for the estimate of longer distances where the measurement errors are inherently larger due to the $\langle 1/r^6 \rangle$ dependence of the measured cross-peak volume.

(B) Coupling-Constant Measurements. The vicinal coupling constants $^3J(\underline{H}NC_\alpha\underline{H})$, $^3J(\underline{C'}NC_\alpha\underline{H})$, $^3J(\underline{H}NC_\alpha\underline{C'})$, and $^3J(\underline{H}NC_\alpha\underline{C}_\beta)$ (Table II) provide additional constraints on the backbone dihedral angle, ϕ, using the generalized Karplus relationships (Karplus, 1959, 1963; Bystrov, 1976). For antamanide, the homonuclear coupling constants $^3J(\underline{H}NC_\alpha\underline{H})$ have been determined from high-resolution E.COSY (Griesinger et al., 1985, 1986) and 2QF-COSY spectra (Piantini et al., 1982). Data sets of 512 × 8192 data points were acquired at five temperatures (270, 280, 300, 308, and 320 K). Using uniformly ^{13}C-labeled antamanide, the heteronuclear coupling constants were determined by heteronuclear relayed E.COSY experiments (J. M. Schmidt, R. R. Ernst, S. Aimoto, and M. Kainosho, unpublished work) and by a selective heteronuclear single-quantum correlation (HSQC) experiment. In addition, ω_1-^{13}C-filtered TOCSY and heteronuclear multiple-bond correlation (HMBC) experiments (Bax & Summers, 1986) were performed, using antamanide samples with a natural isotope abundance.

The heteronuclear coupling constants $^3J(\underline{H}NC_\alpha\underline{C'})$ and $^3J(\underline{H}NC_\alpha\underline{C}_\beta)$ were determined by the heteronuclear relayed E.COSY experiment illustrated in Figure 2a. In comparison to a HMQC-COSY experiment, the coherence-transfer pulse after the evolution period t_1 is replaced by a small-flip-angle pulse. It avoids effects on the passive spins in the ^{13}C-enriched samples.

The pulse delay, $\Delta = 3.57$ ms, controls the evolution of the heteronuclear one-bond couplings. For the small-flip-angle pulse, $\beta = 35°$ was selected. At 600 MHz, the ν_1 and ν_2 spectral widths were set at 9091 and 6250 Hz, with the acquisition times $t_{1max} = 113$ ms and $t_{2max} = 492$ ms. The total experimental time was 36 h, during which FIDs for 2048 t_1 increments were recorded with 6144 data points. J couplings were determined by locating the centers of gravity of the two E.COSY multiplet components and measuring their separation, as will be described elsewhere (J. M. Schmidt, R. R. Ernst, S. Aimoto, and M. Kainosho, unpublished work).

The pulse sequence for the selective heteronuclear single-quantum correlation (HSQC) experiment, shown in Figure 2b, was used for the measurement of $^3J(\underline{C'}NC_\alpha\underline{H})$ and $^3J(\underline{H}NC_\alpha\underline{C'})$ couplings in a ^{13}C-enriched sample of antamanide. The experimental scheme allows the suppression of dispersive peak-shape contributions.

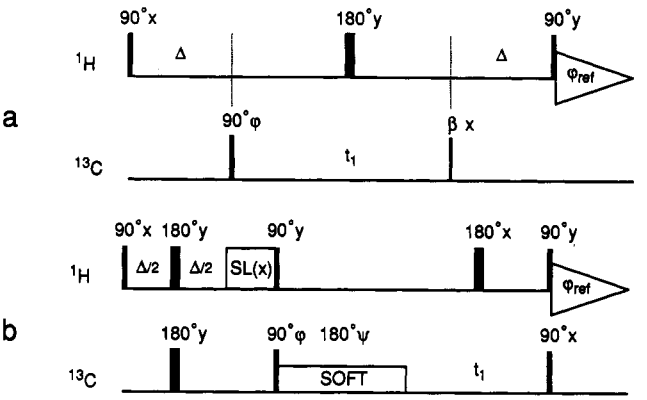

FIGURE 2: Pulse sequences for the determination of heteronuclear (three-bond) J-coupling constants. (a) Heteronuclear relayed E.COSY experiment. The flip angle β_x is small enough (35°) not to affect significantly the passive ^{13}C spins in ^{13}C-enriched samples (J. M. Schmidt, O. W. Sørensen, and R. R. Ernst, unpublished work). The phase cycle is $(\varphi,\varphi_{ref}) = (x,x),(-x,-x)$. (b) Selective heteronuclear single-quantum correlation (HSQC) experiment. The spin-locking (SL) of the protons eliminates dispersive peak contributions. The selective soft π pulse is applied to the ^{13}CO spins for the measurement of $^3J(\underline{C'}NC_\alpha\underline{H})$ and $^3J(\underline{H}NC_\alpha\underline{C'})$ coupling constants. The phase cycle is $(\varphi,\psi,\varphi_{ref}) = (x,x,x), (-x,x,-x), (x,y,-x), (-x,y,x), (x,-x,x), (-x,-x,-x), (x,-y,-x), (-x,-y,x)$.

The experiment starts with a heteronuclear coherence-transfer step that creates (antiphase) coherence exclusively on the carbonyl ^{13}C. Out-of-phase components, caused by proton–proton interactions evolving during the period Δ, are eliminated by spin-locking the proton coherence before the heteronuclear transfer pulses. The coherence on non-carbonyl ^{13}C nuclei is suppressed by phase-cycling the soft π pulse applied to the carbonyl region immediately following the transfer pulses (Wu et al., 1989). The experiment produces an in-phase pattern in the ω_1 dimension and an antiphase pattern with respect to the active heteronuclear coupling in the ω_2 dimension. The active coupling was examined by means of a convolution procedure suggested by Titman et al. (1990) using the peak shape from a homonuclear TOCSY spectrum (Braunschweiler & Ernst, 1983; Bax & Davis, 1985).

The selective 400-MHz HSQC spectrum of antamanide was recorded at 310 K with the pulse sequence of Figure 2b with $\Delta = 41$ ms and a spin-lock time of 2 ms. The soft π pulse, applied on-resonance to the carbonyl ^{13}C spins, consisted of a 50-pulse DANTE sequence of 1-ms duration (Morris & Freeman, 1978). The spectral widths in the ν_1 and ν_2 dimensions were 595 and 4000 Hz with acquisition times of

Table II: Experimental *J*-Coupling Constants of Antamanide (in Hz) Together with rms Error Limits (±)[a]

residue *i*	$^3J(\underline{H}NC_\alpha\underline{H})$[b]			$^3J(\underline{C}'_{i-1}NC_\alpha\underline{H}_i)$			$^3J(\underline{H}NC_\alpha\underline{C}')$			$^3J(\underline{H}NC_\alpha\underline{C}_\beta)$		
	min	exp	max	min	exp	max	min	exp	max	min	exp	max
[1]Val	5.3	7.3 ± 0.2	9.3	0	1–3[c]	4	0.2	1.8 ± 0.2[f]	3.2	0	0.7 ± 0.2	2.5
[2]Pro				0	0–2[d]	2						
[3]Pro				0	1–3[c]	4						
[4]Ala	6.6	8.6 ± 0.2	10.6	0	1–3[c]	4	0	0–2[d]	2	0	1.6 ± 1[h]	3.5
[5]Phe	4.8	6.8 ± 0.2	8.8	2	5.6 ± 1[e]	8	0	2 ± 3[g]	5	0	0.9 ± 0.2[f]	3
[6]Phe	4.6	6.6 ± 0.2	8.6	0	1–3[c]	4	0.4	1.9 ± 0.2[f]	3.4	0	1.0 ± 0.2[f]	3
[7]Pro				0	0–2[d]	2						
[8]Pro				0	1–3[c]	4						
[9]Phe	6.3	8.3 ± 0.2	10.3	0	1–3[c]	4	0	0.5 ± 0.2[f]	2	0	0.8 ± 0.2[f]	3.5
[10]Phe	4.7	6.7 ± 0.2	8.7	2	6.8 ± 1[e]	8	0.5	3.5 ± 3[g]	6.5	0	1.0 ± 0.2[f]	3

[a] In addition, the conservative *J*-coupling-restraint ranges (min, max) used in the structure determination procedure are given. [b] Values in agreement with Müller (1986), Griesinger et al. (1987), and Kessler et al. (1989). [c] Visible cross peak in HMBC experiment; coupling constant not accurately measurable. [d] No cross peak visible in HMBC experiment. [e] Measured from HSQC experiment. [f] Measured with heteronuclear relayed E.COSY experiment. [g] Conflicting results from heteronuclear relayed E.COSY experiment and HSQC experiment. [h] From ω_1-^{13}C-filtered TOCSY experiments at 400 and 600 MHz proton resonance frequency.

163 and 512 ms, respectively. The data were zero-filled to 256 × 16 384 prior to Fourier transformation. For line-shape comparison, a TOCSY spectrum was recorded using a mixing time τ_m = 55 ms and an MLEV-17 mixing sequence with an rf field strength of 6 kHz, preceded and followed by 2-ms trim pulses (Bax & Davis, 1985).

To determine the desired active coupling constant, ν_2 cross sections through the selective HSQC and TOCSY spectra were taken. The (antiphase) HSQC trace was convoluted with an in-phase δ-function doublet of splitting J_{trial}, while the (in-phase) TOCSY trace was convoluted with an antiphase δ-function doublet with the same splitting. J_{trial} was adjusted in an iterative manner to obtain an optimal superposition of the two spectra.

The measured coupling constants were verified using ^{1}H-detected heteronuclear multiple-bond correlation (HMBC) experiments at 256 and 300 K and ^{13}C-detected COLOC (Kessler et al., 1984) experiments at 280, 303, 310, and 320 K using a natural-abundance sample. In the case of the HMBC experiment, 3600 t_1 increments, each of 8 scans, were recorded, with 2048 data points in t_2. For the COLOC experiments, the spectral width was confined to the carbonyl resonances, and data for 334 t_1 increments were collected with 1024 data poins recorded. Delays of 25 and 35 ms were used on either side of the refocusing 180° pulse to emphasize cross peaks due to the long-range heteronuclear ^3J couplings to the carbonyl nuclei. Computer-simulated transfer functions, based on the known homonuclear coupling constants, were consulted to optimize the delays for maximum cross-peak intensity. In addition, ^{13}C-detected *J*-resolved 2D experiments, using selective 180° pulses on the NH or H_α region of the proton spectrum (Bax & Freeman, 1982), were applied to cross-check the coupling constants determined from the two heteronuclear correlation experiments. The measured *J*-coupling constants are summarized in Table II. The table also comprises the upper and lower bounds of *J* values that have been used for the structure determination as described later.

(C) Measurement and Analysis of Relaxation in the Rotating Frame. As mentioned in the introduction, a backbone conformational exchange process was expected for antamanide with lifetimes on the order of microseconds. In this time range, relaxation measurements in the rotating frame are most informative. They are sensitive to processes with exchange rate constants comparable to the applied rf field strength, $\omega_1 = -\gamma B_1$, provided the process modulates a nuclear resonance frequency. In the case of a two-site exchange process with the exchange time constant τ_{ex}, with the populations p_1 and p_2 of the two conformers, and with the resonance frequency difference $\Delta\omega$ between the exchanging sites, one finds (Deverell et al., 1970; Bleich and Glasel, 1978)

$$1/T_{1\rho} = 1/T_{1\rho d} + 1/T_{1\rho ex} \quad (1)$$

$$\frac{1}{T_{1\rho ex}} = \frac{p_1 p_2 \tau_{ex}}{1 + \omega_1^2 \tau_{ex}^2} (\Delta\omega)^2 \quad (2)$$

$1/T_{1\rho ex}$ is the exchange contribution, and $1/T_{1\rho d}$ represents the dipole–dipole relaxation that shows little sensitivity to the conformational exchange process. The latter can be determined by an independent spin–lattice relaxation measurement in the laboratory frame.

The pulse sequence for $T_{1\rho}$ measurements is $(\pi/2)_x$–$\omega_{1eff,y}(\tau_m)$–acquisition. After an initial $(\pi/2)_x$ pulse, the magnetization is spin-locked during the time τ_m along the *y*-axis with an rf field of effective amplitude ω_{1eff}. The latter was varied by using a repetitive pulse sequence of amplitude ω_1 and duty cycle c_d: $\omega_{1eff} = \omega_1 c_d$, giving a range of 1.3 kHz $\leq \omega_{1eff}/2\pi \leq$ 10.3 kHz. The FIDs following the removal of the spin-locking field were Fourier-transformed. The peak intensities determined from the spectrum were fitted with the three-parameter function $I(\tau_m) = I_0 \exp(-\tau_m/T_{1\rho}) + C$. The constant C takes account of a possible baseline shift.

The results of the $T_{1\rho}$ measurements on antamanide are shown in Figure 3 and are summarized in Table III. Figure 3a illustrates the rf field dependence of the proton resonance spectra recorded after a spin-locking time of τ = 100 ms at 300 K. It is apparent that the spectra are insensitive to the applied rf field strength varying from 2.6 to 10.3 kHz with the exception of the NH protons of [1]Val and [6]Phe. Indeed, a careful numerical analysis revealed a significant rf field dependence exclusively for the two mentioned protons. This is supported by the line broadening visible in Figure 3a for these two protons that is indicative of an exchange process.

Three possible origins of the observed rf field dependence of $T_{1\rho}$ have been considered: (a) modulation of the ^{14}N–^{1}H *J*-coupling constant by an exchange process, leading to scalar relaxation of the first kind (Abragam, 1961); (b) ^{14}N quadrupolar relaxation, leading through the ^{14}N–^{1}H *J* coupling to scalar relaxation of the second kind (Abragam, 1961); and (c) modulation of the proton chemical shift by a conformational exchange process. The first two possibilities can be excluded by experiments as follows: (a) A measurement of the ^{15}N–^{1}H *J*-coupling constants via observation of natural-abundance ^{15}N resonance revealed values within the narrow range 90.0 $\leq {}^1J(^{15}NH) \leq$ 93.0 Hz for all NH fragments in antamanide at the mentioned temperatures. These are typical values for tightly bonded protons, consistent with values observed in

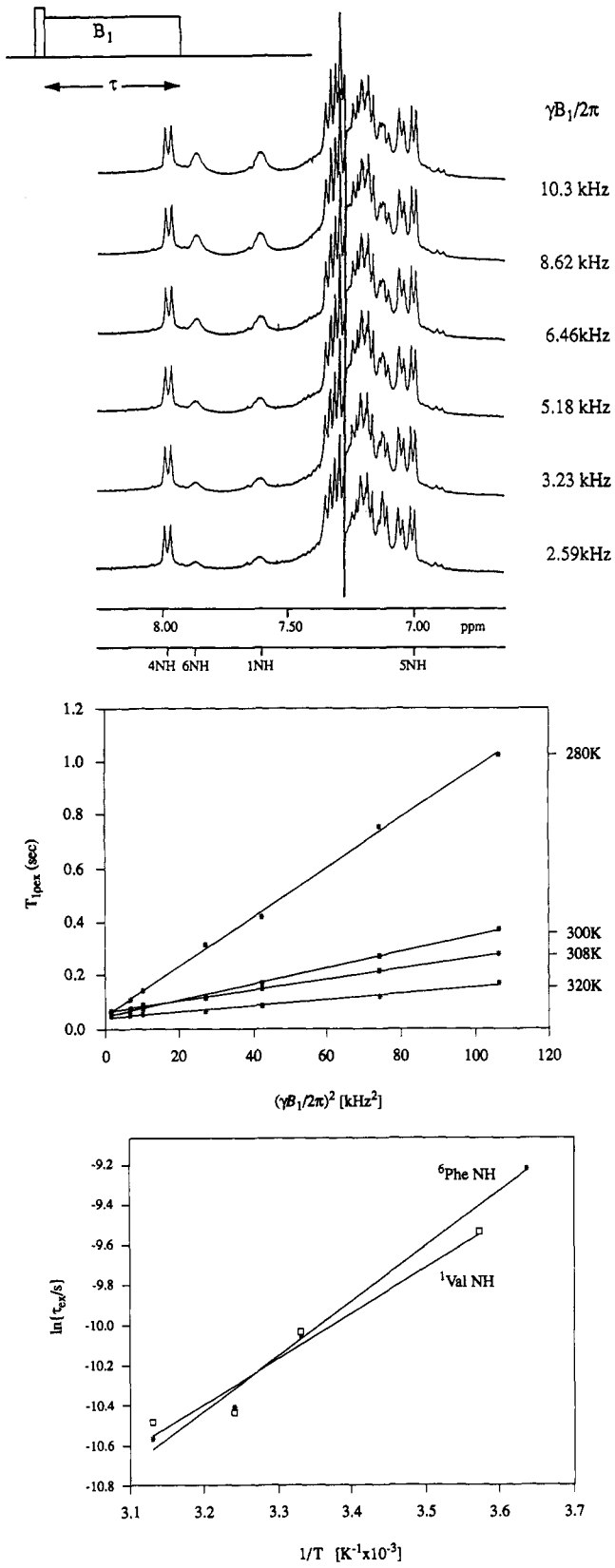

FIGURE 3: $T_{1\rho}$ experiments. (a, top) Spectra demonstrating the B_1-field dependence of the rotating frame relaxation rates for NH and aromatic resonances. The spectra shown result from free induction decays collected after spin-locking for 100 ms at six different B_1 field strengths and $T = 300$ K. (b, middle) Exchange contribution to $T_{1\rho}$, $T_{1\rho ex}$ as a function of $(\gamma B_1/2\pi)^2$ for the NH resonance of ^{1}Val at 280, 300, 308, and 320 K. Linear regression was used to fit the data to eq 2. (c, bottom) Dependence of the exchange lifetime, τ_{ex}, on the inverse temperature for ^{1}Val NH and ^{6}Phe NH.

proteins. A proton-exchange process would necessarily lead to a reduced coupling constant according to the fractional

Table III: Proton $T_{1\rho}$ Relaxation Times for Different rf Field Strengths and T_1 Relaxation Times at Four Temperatures for ^{1}Val NH and ^{6}Phe NH[a]

		^{1}Val NH			
		T (K)			
	$\gamma B_1/2\pi$ (kHz)	280	300	308	320
$T_{1\rho}$ (ms)	1.3	44	50	55	40
	2.6	68	52	60	42
	3.2	81	58	71	45
	5.2	120	82	87	53
	6.5	133	108	108	68
	8.6	155	143	141	91
	10.3	164	168	166	120
T_1 (ms)		400	420	530	550
		^{6}Phe NH			
		T (K)			
	$\gamma B_1/2\pi$ (kHz)	275	300	308	320
$T_{1\rho}$ (ms)	1.3	31	44	45	50
	2.6	43	41	53	55
	3.2	70	46	53	60
	5.2	78	72	76	72
	6.5	99	93	94	80
	8.6	131	131	120	111
	10.3	141	152	147	135
T_1 (ms)		410	420	530	510

[a] Repeated measurements of $T_{1\rho}$ and T_1 gave standard deviations of 7.5% and 5.0%, respectively.

residence time. Such a process can thus be excluded on a time scale relevant for $T_{1\rho}$ relaxation. (b) Quadrupolar relaxation of ^{14}N depends on the electric field gradient at the nuclear site and on the random reorientation processes. There is no obvious reason to assume that the electric field gradients at the various ^{14}N sites are sufficiently different to explain the observed differential $T_{1\rho}$ effects.

The remaining explanation of the $T_{1\rho}$ data is a conformational exchange process that induces a modulation of the chemical shifts of the NH protons of ^{1}Val and ^{6}Phe and leads to a relaxation rate constant according to eq 1. As seen from eq 1, $T_{1\rho}$ depends on three unknown parameters: the exchange time constant, τ_{ex}; the product of the population numbers and the chemical shift difference, $(p_1p_2)^{1/2}\Delta\omega$; and the dipolar relaxation time, $T_{1\rho d}$. Thus, a three-parameter fit is required to analyze the ω_1 dependence tabulated in Table III. To increase the accuracy of the determination of τ_{ex}, we derive $T_{1\rho d}$ from a measurement of T_{1d} in the laboratory frame. We assume as a simplified model an isotropically tumbling system of two identical spins with internuclear separation r. The dipolar contributions to T_1 and $T_{1\rho}$ are given by (Abragam, 1961)

$$1/T_{1d} = \frac{3}{20}\left[\frac{\mu_0\gamma^2\hbar}{4\pi r^3}\right]^2\Big(J(\omega_0) + 4J(2\omega_0)\Big) \qquad (3)$$

$$1/T_{1\rho d} = \frac{3}{20}\left[\frac{\mu_0\gamma^2\hbar}{4\pi r^3}\right]^2\Big(\frac{3}{2}J(0) + \frac{5}{2}J(\omega_0) + J(2\omega_0)\Big) \qquad (4)$$

where $J(\omega) = 2\tau_c/(1 + (\omega\tau_c)^2)$. The two expressions can only be related to each other when the ratio of the $J(\omega)$-dependent factors or the rotational correlation time, τ_c, is known. The former can be determined by a combined T_1 and $T_{1\rho}$ measurement for any proton that is not affected by a slow intramolecular motional process. The latter can be determined most conveniently from a $^{13}C_\alpha$ T_1-relaxation measurement. Assuming that it is dominated by the dipolar interaction to the directly bonded proton, $T_1(^{13}C_\alpha)$ is given by (McCain et

Table IV: T_1 Relaxation Times (in ms) of α Carbons in Antamanide at 125-MHz ^{13}C Resonance Frequency[a]

	T (K)			
	256	300	308	320
^{1}Val	/	480	/	/
^{2}Pro	200	328	398	440
^{3}Pro	218	404	417	470
^{4}Ala	/	448	/	/
^{5}Phe	277	479	453	/
^{6}Phe	/	408	483	471
^{7}Pro	/	432	/	/
^{8}Pro	/	340	/	/
^{9}Phe	265	394	/	407
^{10}Phe	281	405	/	429
$\tau_c(C_\alpha)$ (ns)	0.51	0.18	0.15	0.15
τ_c(NH) (ns)	0.57	0.17	0.13	0.13

[a] Inability to measure T_1 due to spectral overlap is signified by /. Rotational correlation times, $\tau_c(C_\alpha)$, deduced from $T_1(C_\alpha)$ and τ_c(NH) deduced from a comparison of T_{1d} and $T_{1\rho d}$ for nonexchanging NH protons are also given.

al., 1988)

$$1/T_{1C} = \frac{3}{20}\left[\frac{\mu_0\gamma_H\gamma_C\hbar}{4\pi r_{CH}^3}\right]^2\left(\frac{1}{3}J(\omega_H-\omega_C) + J(\omega_C) + 2J(\omega_H+\omega_C)\right) \quad (5)$$

By use of this equation, it is possible to compute τ_c from a $T_1(C_\alpha)$ measurement, assuming an internuclear C_α–H_α distance of 1.08 Å (including vibrational averaging effects; McCain et al., 1988).

The carbon-13 spin–lattice relaxation rates, required for the evaluation of eq 5, were measured with the inversion–recovery sequence (relaxation delay)–π–τ–(π/2)–acquisition. Broad-band proton decoupling was applied during acquisition, while low-level proton irradiation led to NOE signal enhancement during the relaxation delay. One thousand scans per delay time were collected. Peak heights were measured and fitted by the three-parameter function $I(\tau) = I_0(1 - 2A\exp(-\tau/T_1))$. The lowest measured value of $T_1(C_\alpha)$ was used to compute τ_c because, in the motional regime investigated here, the effects of additional internal motions will tend to lengthen the effective relaxation time. The $T_1(C_\alpha)$ values for five temperatures and the corresponding correlation times are given in Table IV together with τ_c values computed from the ratio of the relaxation times T_{1d} and $T_{1\rho d}$ of nonexchanging NH protons, K, given by equations 3 and 4.

$$K = \frac{T_{1d}}{T_{1\rho d}} = \left[\frac{3}{2}J(0) + \frac{5}{2}J(\omega_0) + J(2\omega_0)\right] \Big/ \left[J(\omega_0) + 4J(2\omega_0)\right] \quad (6)$$

The results in Table IV agree with the estimation of τ_c from the observed zero-crossing of NOE cross-peak intensities at approximately 280 K where $\omega_0\tau_c \sim 1.12$, leading for $\omega/2\pi$ = 400 MHz to $\tau_c \simeq 400$ ps. Previously, a value of $\tau_c \simeq 300$ ps was obtained at 280 K also from ^{13}C T_1 measurements (Mádi et al., 1990).

The exchange lifetime, τ_{ex}, can be derived by fitting $T_{1\rho}$(NH), after elimination of T_{1d}, by a linear function with respect to ω_1^2, as implied by equations 1 and 2:

$$T_{1\rho ex} = A\omega_1^2 + B \quad (7)$$

where $A = \tau_{ex}/(p_1p_2\Delta\omega^2)$ and $B = 1/(p_1p_2\Delta\omega^2\tau_{ex})$. From the optimized values A and B, one then obtains $\tau_{ex} = (A/B)^{1/2}$ and $(\Delta\omega)^2p_1p_2 = (AB)^{1/2}$. Four fits for $T_{1\rho ex}$ of the ^{1}Val NH resonance at 280, 300, 308, and 320 K are shown in Figure 3b. The results for ^{1}Val NH and ^{6}Phe NH are collected in Table V. The exchange lifetime, τ_{ex}, exhibits a temperature dependence which can be fitted to an Arrhenius-type relationship of the form

Table V: Exchange Lifetimes, τ_{ex}, and $4p_1p_2\Delta\nu^{app}$ Parameters for ^{1}Val NH and ^{6}Phe NH

		T (K)				
		275	280	300	308	320
^{1}Val NH	τ_{ex} (μs)		73.4	42.9	29.6	28.4
	$4p_\alpha p_\beta\Delta\nu^{app}$ (Hz)		177	238	243	315
^{6}Phe NH	τ_{ex} (μs)	99.5		43.5	30.0	25.8
	$4p_\alpha p_\beta\Delta\nu^{app}$ (Hz)	259		263	268	275

$$\ln \tau_{ex} = C - E_a/(RT) \quad (8)$$

as shown in Figure 3c. One finds, for ^{1}Val NH, τ_{ex} = 28 μs at 320 K, τ_{ex} = 73 μs at 280 K, and E_a = 19 kJ mol^{-1} and, for ^{6}Phe NH, τ_{ex} = 26 μs at 320 K, τ_{ex} = 100 μs at 275 K, and E_a = 23 kJ mol^{-1}. These values are in agreement with the mentioned line broadening in Figure 3a caused by a transverse relaxation time, T_2, that is related to $T_{1\rho}$ by $T_2 = \lim_{\omega_1\to 0} T_{1\rho}$.

The chemical shift difference, $\Delta\omega$, between the two sites cannot be separated from the populations p_1 and p_2. However, if we assume equipopulated sites, $p_1 = p_2 = 0.5$, irrespective of temperature, the apparent chemical shift difference between the two exchanging sites for ^{1}Val NH linearly increases from $\Delta\nu^{app}$ = 177 Hz at 280 K to 315 Hz at 320 K. The apparent chemical shift difference between the two exchanging sites for ^{6}Phe NH, on the other hand, has a smaller temperature dependence and varies from 259 to 275 Hz. The temperature dependence of the chemical shifts of the other NH protons is also linear: the ^{4}Ala NH and ^{9}Phe NH resonances move downfield, and the ^{5}Phe NH and ^{10}Phe NH resonances move upfield, with increasing temperature.

At this stage, it is not possible to uniquely identify the nature of the exchange process. However, it is likely that it involves the breaking and forming of hydrogen bonds of the NH protons of ^{1}Val and ^{6}Phe. Additional hydrogen bonds seem not to be affected by the conformational exchange, although it cannot be excluded that a hydrogen bond breaking and forming process could remain unobservable due to accidentally equal chemical shifts in the two states.

Molecular Modeling Methods: MEDUSA Conformational Search Procedure. The MEDUSA algorithm extends the conformational search capability from single-conformational to multiconformational systems (Brüschweiler et al., 1991). The method systematically generates conformers which may individually violate some experimental constraints that can be satisfied, however, by an ensemble of rapidly exchanging conformations.

The MEDUSA search procedure relies on the strong $1/r_{i,k}^6$ internuclear distance dependence of the cross-relaxation rate constants. In a conformational equilibrium with $\tau_{ex} > \tau_c$, normally the conformation, c, with the shortest $r_{i,k}^{(c)}$ determines the NOE cross-peak intensity,

$$I_{i,k} = (\text{const})\sum_c p^{(c)}/(r_{i,k}^{(c)})^6 \quad (9)$$

unless the corresponding population $p^{(c)}$ is very low. This implies that each conformation is associated with a set of distance constraints that primarily reflect the geometry of this substate. By a systematic application of the distance constraints, it is possible to find compatible subsets of DCs that determine individual conformations. It should be noted

that this feature is not shared by the angular constraints, as the Karplus relations (Karplus, 1959, 1963) involve much smoother and periodic functions such that each angular constraint is significantly influenced by several or all of the conformations taking part in the dynamic equilibrium.

Distance constraints are interpreted in the following manner: The detection of an NOE/ROE yielding a DC with the nominal distance $r_{k,l}^{NOE}$ implies that there is a conformation in the dynamic equilibrium in which the proton pair (k, l) has a distance $r_{k,l} \leq r_{k,l}^{NOE}$. In contrast, an ADC signifies that there is no 100% populated conformation ($p_c = 1$) with an internuclear separation $r_{k,l} < r_{thres}$, where r_{thres} is the maximum detectable distance which depends on the signal-to-noise ratio and on the NOESY performance conditions (we select here $r_{thres} = 3.7$ Å). For less populated conformations, $p_c < 1$, the exclusion distance becomes even smaller, i.e., there is no conformation with $r_{k,l} < r_{thres}\, p_c^{1/6}$.

The algorithm consists of two parts. At first, a large number of rigid conformations is generated, each of which fulfills a subset of the DCs, fulfills all ADCs, and has an energy below a set threshold. In a second step, the conformations are combined in pairs, triples, or larger clusters to fulfill all constraints including all DCs, ADCs, J couplings, and $T_{1\rho}$ data. The conformations are created as follows:

(1) An initial conformation, S, is chosen from a set of possibilities, such as the X-ray structure, structures from molecular dynamics simulations, and structures chosen by a Monte Carlo procedure.

(2) A randomly permuted list of the experimental DCs is established, and the first DC is selected from this list.

(3) An energy threshold, E_{thres}, is chosen randomly within a preset interval $[E_{min}, E_{max}]$. (This avoids the difficult choice of a fixed threshold that may be either too loose or too restrictive.)

(4) The selected DC (e.g., acting between spins I_k and I_l), together with all previous DCs, is added to the molecular force field of CHARMM (Brooks et al., 1983) in the form of a semiparabolic energy term designed to strongly constrain this distance and all previously retained DCs:

$$E_{k,l}(r_{k,l}) = \begin{cases} k(r_{k,l} - r_{k,l}^{NOE})^2, & \text{if } r_{k,l} \geq r_{k,l}^{NOE} \\ 0, & \text{if } r_{k,l} < r_{k,l}^{NOE} \end{cases} \quad (10)$$

An energy minimization, e.g., with 500 steps of ABNR (adapted base Newton–Raphson algorithm; Brooks et al., 1983), yields a new conformation, S′. Its energy, E', is determined in the absence of distance constraints: (a) If $E' < E_{thres}$, S is set equal to S′. (b) If $E' > E_{thres}$, the tested (and violated) DC is removed from the list and from the potential.

(5) The next DC is selected from the list of step 2, and step 4 is repeated. When the list of DCs is exhausted, the conformation S is energy-minimized again, this time for a potential that includes all accepted DCs and all ADCs, the latter also in the form of semiparabolic energy terms. The coordinates of the resulting conformation are stored, together with the list of accepted DCs, and the procedure is continued at step 2 or, less frequently, at step 1.

It should be stressed that the energy-minimization procedure is used here as a tool to drive the molecule through conformational space in order to reach a conformation that fulfills a limited set of distance constraints. The energy calculation used to accept or reject the generated conformation is performed in the absence of the restraining potential. The order in which the randomized DC sequence is applied strongly influences the resultant structure.

When a sufficient number of conformations (usually at least several hundred for peptides like antamanide) have been generated in this manner, all possible combinations, each containing N_S conformations (in practice, $N_S = 2, 3$, or rarely more), are formed. Each combination is tested as a potential exchange system with yet unknown populations, p_α, of the N_S conformations. The populations p_α are optimized to minimize, in the dynamic average, the deviations from the experimental distance and J-coupling constraints (leading to angular constraints, or ACs, using the relations in footnote b of Table VIIb). For this purpose, the weighted mean square error, Q, called the mismatch parameter, is computed:

$$Q = A\sum_{(k,l)}\left\{\sum_{\alpha}^{N_S} p_\alpha J_{k,l}^{\alpha} - J_{k,l}^{exp}\right\}^2 + B\sum_{(k,l)}\left\{\sum_{\alpha}^{N_S} p_\alpha (r_{k,l}^{\alpha})^{-6} - (r_{k,l}^{NOE})^{-6}\right\}^2 \quad (11)$$

where

$$A = 3q\left[\sum_{(k,l)} (J_{k,l}^{exp})^2\right]^{-1}$$

and

$$B = 3(1-q)\left[\sum_{(k,l)} (r_{k,l}^{NOE})^{-12}\right]^{-1}$$

The constants A and B normalize the relative contributions of the angular and distance terms; the arbitrary factor 3 is incorporated so that the majority of pairs produces values within the range $0 \leq Q \leq 1$. The factor q, $0 \leq q \leq 1$, allows one to shift the emphasis between angular and distance constraints. For eq 11 it is assumed that the conformational exchange dynamics is slow compared to the correlation time, τ_c. The optimal populations may be calculated by minimizing the mismatch parameter, Q, with respect to all p_α's.

In a last step, the found conformational equilibrium systems with a low mismatch parameter, Q, are checked for consistency with all further available data, including rotating frame relaxation times, in order to sort out the most probable candidates on the basis of all knowledge available. It is also possible to apply at one stage a maximum deviation criterion to eliminate those conformational exchange systems that give a low average mismatch parameter, Q, but show an unreasonably large deviation for one or a few of the experimental measurements.

RESULTS

The MEDUSA algorithm, as described in the previous section, has been applied to the distance constraints contained in Table I, using the seven starting structures A–G of antamanide given in Table VI. The successive introduction of the randomly ordered constraints led to an ensemble of 936 conformations that form the basis for the construction of dynamic equilibrium systems to model antamanide in chloroform solution.

Analysis of the Ensemble of Conformations. To obtain a survey over the 936 obtained conformations, the ensemble is analyzed with respect to its homogeneity. The conformations are grouped in classes using a root mean square criterion for the deviations of the backbone angles ϕ_i and ψ_i of residue i between two conformations, α and β (Karpen et al., 1989):

$$f_{\alpha,\beta}(\phi,\psi) = \left[\frac{\sum_{i=1}^{n}[(\phi_i^{\alpha} - \phi_i^{\beta})^2 + (\psi_i^{\alpha} - \psi_i^{\beta})^2]}{2n-1}\right]^{1/2} \quad (12)$$

where $n = 10$ for antamanide. Two structures, α and β, are considered to belong to the same class when $f_{\alpha,\beta} \leq f_{threshold}$.

Table VI: Backbone Dihedral Angles ϕ and ψ (in Degrees) of the Seven Starting Conformations A–G in the MEDUSA Algorithm

	conformation[a]													
	A		B		C		D		E		F		G	
residue	ϕ_i	ψ_i	ϕ_i	ψ_i	ϕ_i	ψ_i	ϕ_i	ψ_i	ϕ_i	ψ_i	ϕ_i	ψ_i	ϕ_i	ψ_i
[1]Val	−110	−177	−103	152	26	72	−143	161	−92	150	−120	178	−124	62
[2]Pro	−85	155	−69	152	−75	141	−82	128	−81	148	−97	139	−102	168
[3]Pro	−95	44	−92	−7	−96	27	−109	57	−90	−6	−105	27	−103	38
[4]Ala	−112	−54	−91	−32	−96	−36	−136	101	−109	60	−128	49	−128	33
[5]Phe	91	−40	72	21	76	−6	−118	77	−47	92	−21	69	−16	43
[6]Phe	−108	−167	−82	151	−58	119	−136	109	−143	167	−127	−176	−119	−168
[7]Pro	−81	149	−73	154	−71	148	−66	131	−82	124	−107	116	−59	78
[8]Pro	−97	51	−87	−5	−89	19	−93	10	−91	−15	−109	40	−93	25
[9]Phe	−109	−59	−91	−33	−93	−41	−98	104	−84	63	−120	43	−114	−53
[10]Phe	89	−38	70	31	72	−28	−118	98	−64	35	−47	62	−1	−40

[a] (A) Structure resulting from the midpoint of a 1-ns molecular dynamics run performed using CHARMM and subject to constraint-free energy minimization. (B) Structure obtained after constraint-free energy minimization of the X-ray structure (Karle et al., 1979). (C) Structure resulting from the end point of a 1-ns molecular dynamics run performed using CHARMM and subject to constraint-free energy minimization. (D) Arbitrarily selected structure resulting from a previous run of the MEDUSA algorithm. (E) Structure proposed by Kessler et al. (1989b) (from an rMD run) subjected to additional constraint-free energy minimization. (F), (G) Arbitrarily selected structures resulting from the same run of the MEDUSA algorithm as for structure D.

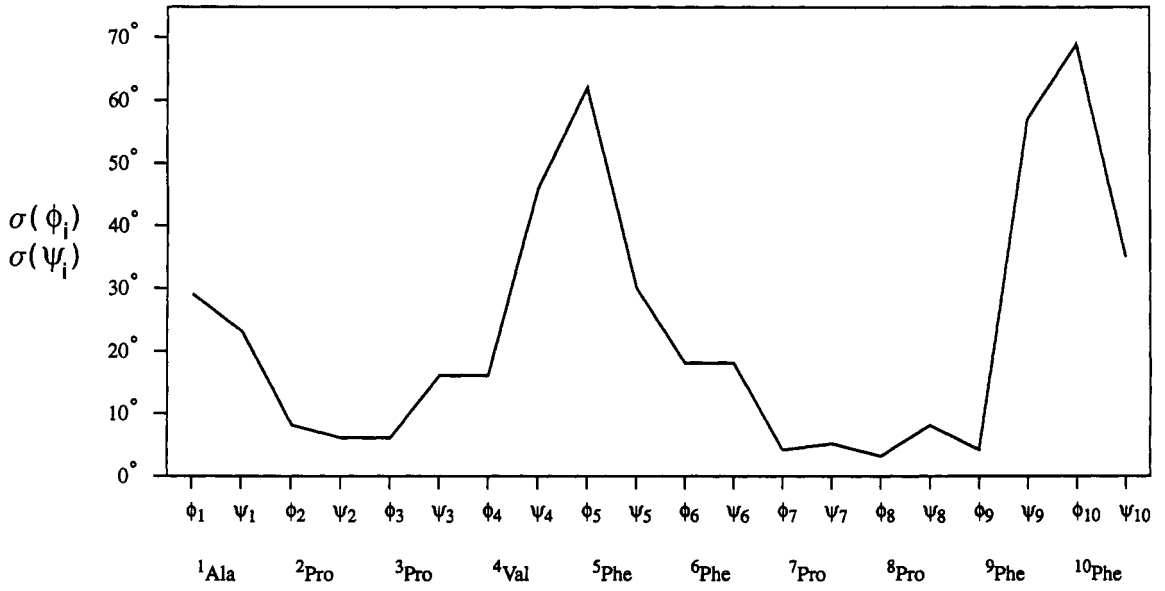

FIGURE 4: Standard deviations of the angles ϕ_i and ψ_i for the entire ensemble of conformations plotted against the residue number.

In this procedure, the first conformation is selected from a randomly ordered list. It becomes the template for the first class and is compared with all other conformations with respect to the above criterion to select its class partners. The template for the next class is formed by the first yet uncategorized structure in the list, and the procedure is repeated until all conformations are classified.

For threshold values $f_{\text{threshold}}$ = 3°, 10°, 20°, and 30°, one finds 255, 75, 24, and 12 classes, respectively. Although this classification depends on the arrangement of the conformations in the original list, we have observed the same characteristic dependence for differently sorted lists. It was found that strongly differing initial structures contributed to the same class. This illustrates that the sequential application of the structural constraints forces the molecule into regions of conformational space that are more dependent on the order of the applied constraints than on the starting conformation.

The angular standard deviations of the entire ensemble of conformations, plotted in Figure 4, reveal that the structures are least well defined in the regions ψ_4,ϕ_5,ψ_5 and ψ_9,ϕ_{10}, ψ_{10},ϕ_1,ψ_1, i.e., in regions adjacent to the mobile protons [1]Val NH and [6]Phe NH. On the other hand, the intermediate regions $\phi_2,\psi_2,\phi_3,\psi_3,\phi_4$ and $\phi_6,\psi_6,\phi_7,\psi_7,\phi_8,\psi_8,\phi_9$ show significantly less variation. This can be taken as a preliminary indication of flexibility in the regions ψ_4,ϕ_5,ψ_5 and $\psi_9,\phi_{10},\psi_{10},\phi_1,\psi_1$.

Search for Conformational Exchange Systems Compatible with the Experimental Data. The search has been limited to two-site conformational exchange systems. This seems sensible, taking into account the limited amount of data to define the backbone structures of the exchanging conformations. All 32 385 possible pairs of the 255 class structures that represent classes with a maximum mean backbone angular deviation of $f_{\text{threshold}}$ = 3° have been investigated. A histogram of the number of pairs versus their Q values is presented in Figure 5a. It is seen that the distribution is unimodal with a mean value of $Q \simeq 0.54$. The optimum conformational pair reaches a value of $Q = 0.22$. It is interesting to note that the minimum value of Q assumed by a single rigid conformation is $Q = 0.50$.

Consideration of the Hydrogen-Bonding Network. On the basis of the measured $T_{1\rho}$ data, we postulate, as discussed before, that [1]Val NH and [6]Phe NH must be involved in a hydrogen bond breaking and forming process caused by the conformational dynamics. Thus only those pairs of structures shall be retained that differ in the hydrogen-bonding network at [1]Val NH and [6]Phe NH. No restrictions will be imposed on the connectivity at other NH protons. Dynamics at these points might have, by chance, a negligible effect on the NH chemical shift and remain unnoticed in a $T_{1\rho}$ measurement.

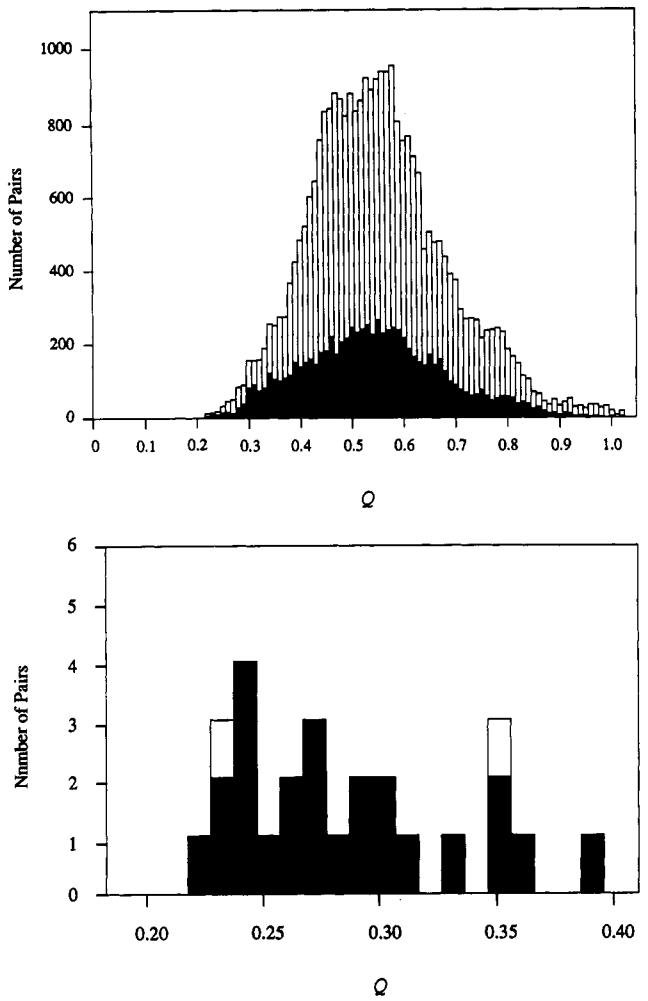

FIGURE 5: Histograms of the conformational exchange pairs of antamanide based on the 255 class structures with $f_{threshold} = 3°$ versus their Q values according to equations 11 and 12. (a, top) Open rectangles represent all 32 385 possible pairs; the filled areas represent the pairs that conform, in addition, to the hydrogen bond dynamics in agreement with the $T_{1\rho}$ measurements. (b, bottom) Histogram of the 26 pair structures that conform to the maximum deviation criterion described in the text. The filled areas represent the 24 structures that agree, in addition, to the hydrogen bond dynamics suggested by the $T_{1\rho}$ measurements.

To localize the hydrogen bonds, a search has been performed by using CHARMM to determine the hydrogen bond connectivity for each conformation. Those conformational pairs that show identical connectivity at one or both of the mentioned amide protons have been rejected, leading to the more restricted histogram superimposed upon Figure 5a. It is apparent that the number of surviving pairs is reduced by a factor of 3. The most common hydrogen bond networks of the pairs with a small mismatch parameter, Q, are illustrated in Figure 6. It is seen that many of them involve the breaking and forming of two specific hydrogen bonds, ^{1}Val NH·^{9}Phe CO and ^{6}Phe NH·^{4}Ala CO. It is likely that these are responsible for the observed $T_{1\rho}$ behavior.

It has been recognized by Kessler et al. (1988, 1989b) that the most dominant conformational changes occur near the dihedral angles ϕ_5 and ϕ_{10}, which may assume positive and negative values due to conformational interconversion. Accordingly, it is possible to characterize the relevant conformations by the sign pair of ϕ_5 and ϕ_{10}. Typical values for these angles are also included in Figure 6. The structural pairs P1, P3, P4, P5, and P6 are of the *syn*-correlated flipping type, (+ +) ↔ (– –), while P2 has an *anti*-correlated flipping character, (– +) ↔ (+ –). In P7 and P8, only one of the two angles changes sign.

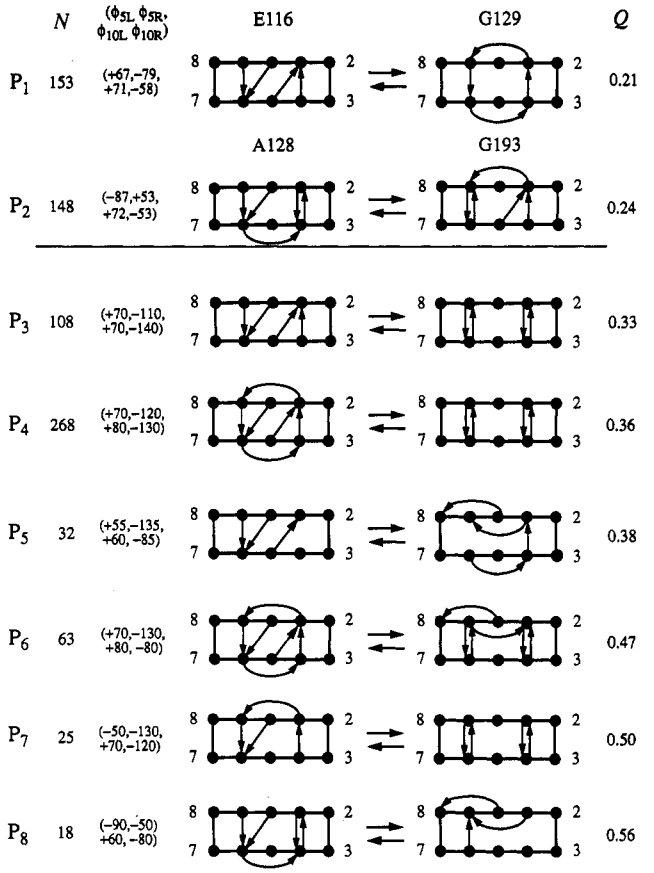

FIGURE 6: Most common hydrogen-bonding networks of low-Q structural pairs in the ensemble of 815 pair structures obtained with the loosened maximum deviation criteria $R_1 = 0.7$ and $R_2 = 1.4$ (eq 14) and the J-value constraints given in Table II. An NH·OC hydrogen bond is defined by an N–O distance of less than 3.4 Å and an NHO angle of more than 105°. The arrows point from NH to OC. The structures P_1 (*syn*-pair) and P_2 (*anti*-pair) conform also to the more stringent maximum deviation criteria discussed in the text that lead to Figure 5b. Also shown are the occurrence numbers, N, of the pairs, the characteristic ϕ_5 and ϕ_{10} angles, and the mismatch parameter values, Q.

Maximum Deviation Criteria. To further narrow down the set of pair structures, only those pairs are retained where, in addition to a low rms error, the deviation for each individual parameter is below a preset threshold value. This avoids the consideration of pairs in which the fulfillment for most of the constraints masks the strong violation of an individual constraint. We require for the conformationally averaged distance, $r^{av}_{k,l}$, and the averaged coupling constant, $J^{av}_{k,l}$, that

$$J^{min}_{k,l} \leq J^{av}_{k,l} \leq J^{max}_{k,l} \tag{13}$$

and

$$\left[\frac{1}{R_2 r^{exp}_{k,l}}\right]^6 \leq \left[\frac{1}{r^{av}_{k,l}}\right]^6 \leq \left[\frac{1}{R_1 r^{exp}_{k,l}}\right]^6 \tag{14}$$

where the limit factors chosen are $R_1 = 0.85$ and $R_2 = 1.20$. The J-coupling limits applied are given in Table II.

This procedure drastically reduces the number of pair structures, and only 26 remain, of which 24 feature a hydrogen-bonding network dynamics compatible with the $T_{1\rho}$ data. The corresponding histogram is shown in Figure 5b. All of the 24 pair structures conform to the two hydrogen-bonding networks P_1 and P_2, shown at the top of Figure 6. Twenty pairs belong to the P_1 type with minor differences in their geometries; all of them involve *syn*-correlated (+ +) ↔ (– –) flipping of the angles ϕ_5 and ϕ_{10}. The remaining four pairs are of type P_2 and involve *anti*-correlated (– +) ↔ (+ –) flipping.

Table VII: Characteristics of the Pair Structures P_1 and P_2

(a) Dihedral Angles (in Degrees),[a] Populations, and Conformational Energy

structure	P_1				P_2				X-ray		rMD	
	ϕ_i^{E116}	ϕ_i^{G129}	ψ_i^{E116}	ψ_i^{G129}	ϕ_i^{A128}	ϕ_i^{G193}	ψ_i^{A128}	ψ_i^{G193}	ϕ_i	ψ_i	ϕ_i	ψ_i
[1]Val	−79	−97	127	146	−96	−105	105	162	−112	158	−114	118
[2]Pro	−72	−76	143	133	−70	−80	133	148	−64	161	−58	133
[3]Pro	−96	−106	20	43	−93	−95	17	24	−79	−20	−90	3
[4]Ala	−93	−134	−45	67	−98	−93	83	−49	−103	−22	−90	88
[5]Phe	67	−79	35	63	−87	53	40	27	70	29	−87	96
[6]Phe	−89	−96	126	135	−88	−140	130	135	−78	161	−122	150
[7]Pro	−76	−80	142	140	−68	−72	144	138	−62	160	−74	129
[8]Pro	−93	−95	17	18	−92	−86	22	5	−92	−4	−91	−1
[9]Phe	−95	−112	−42	54	−96	−100	−54	57	−101	−22	−81	81
[10]Phe	71	−58	19	71	72	−53	25	−4	56	48	−83	78
populations	p(E116) = 0.49		p(G129) = 0.51		p(A128) = 0.54		p(G193) = 0.46					
conformational energy (kJ mol^{-1})	E(E116) = 903		E(G129) = 882		E(A128) = 889		E(G193) = 941					

(b) Computed Average J-Coupling Constants for the Conformational Pairs P_1 and P_2 and for an Equally Populated Four-State Equilibrium Combining P_1 and P_2[b]

	P_1				P_2				(P_1, P_2)			
	J_1	J_2	J_3	J_4	J_1	J_2	J_3	J_4	J_1	J_2	J_3	J_4
[1]Val	8	0	2	2	9	0	3	1	9	0	2	2
[2]Pro			0				1				1	
[3]Pro			3				3				3	
[4]Ala	10	0	3	1	9	0	3	1	9	0	3	1
[5]Phe	8	1	7	2	8	2	7	2	8	2	7	2
[6]Phe	9	0	2	2	9	1	2	1	9	0	2	1
[7]Pro			1				0				0	
[8]Pro			3				2				2	
[9]Phe	10	0	3	1	9	0	3	2	10	0	3	1
[10]Phe	6	2	5	3	6	3	6	2	6	2	6	2

[a] Including ϕ angles of the X-ray structure (Karle et al., 1979) and of an rMD structure (Kessler et al., 1989b). [b] These values can be compared with the experimental values given in Table II. The couplings are identified as $J_1 = {}^3J(\underline{\mathrm{H}}\mathrm{NC}_\alpha\underline{\mathrm{H}})$, $J_2 = {}^3J(\underline{\mathrm{H}}\mathrm{NC}_\alpha\underline{\mathrm{C}}')$, $J_3 = {}^3J(\underline{\mathrm{C}}'\mathrm{NC}_\alpha\underline{\mathrm{H}})$, and $J_4 = {}^3J(\underline{\mathrm{H}}\mathrm{NC}_\alpha\underline{\mathrm{C}}_\beta)$ and have been computed by using the relation $J_k(\delta_k) = A_k\cos^2\delta_k + B_k\cos\delta_k + C_k$ with the relevant dihedral angles, δ_k, and the coefficients (in Hz) $A_1 = 9.4$, $B_1 = -1.1$, $C_1 = 0.4$, $A_2 = 5.7$, $B_2 = -2.7$, $C_2 = 0.1$, $A_3 = 9.0$, $B_3 = -4.4$, $C_3 = -0.8$, $A_4 = 4.7$, $B_4 = -1.5$, $C_4 = -0.2$ (Bystrov, 1976).

Table VIII: Internuclear Distances in the Pair Structures P_1 and P_2 and Computed Cross-Peak Volumes (with the Same Normalization as in Table I) for P_1, P_2, and the Four-State Combination (P_1, P_2)

	P_1			P_2			(P_1, P_2)
	distance (Å)		cross-peak	distance (Å)		cross-peak	cross-peak
proton pair	E116	G129	vol	A128	G193	vol	vol
6NH–6H$_\alpha$	2.90	2.93	163	2.91	2.97	155	159
4NH–4H$_\alpha$	2.93	2.96	153	2.95	2.93	154	153
4NH–3H$_\alpha$	3.25	2.94	121	3.29	3.21	85	104
6NH–5H$_\alpha$	2.80	2.59	271	2.76	2.81	216	244
4NH–2H$_\alpha$	2.72	2.82	222	2.70	2.54	311	266
6NH–10H$_\alpha$	3.30	3.30	77	3.30	3.16	88	84
1NH–5H$_\alpha$	3.50	3.11	83	3.06	3.50	90	87
1NH–10H$_\alpha$	3.04	2.67	204	2.93	3.19	128	166
10NH–9H$_\alpha$	3.64	2.82	124	3.65	2.82	114	119
10NH–10H$_\alpha$	2.19	2.42	694	2.18	2.42	730	714
10NH–7H$_\alpha$	3.10	3.74	73	3.51	3.10	81	77
1NH–1H$_\alpha$	2.79	2.90	189	2.95	2.97	149	170
5NH–2H$_\alpha$	3.10	4.66	59	4.61	3.11	57	58
5NH–4H$_\alpha$	3.61	2.49	239	2.34	3.64	346	292
5NH–5H$_\alpha$	2.19	2.83	537	2.87	2.21	494	516
9NH–7H$_\alpha$	2.65	2.70	272	2.65	2.70	275	273
2H$_\alpha$–3H$_\alpha$	2.23	2.07	1050	2.21	2.26	808	927
7H$_\alpha$–8H$_\alpha$	2.27	2.17	848	2.19	2.30	800	825
5H$_\alpha$–10H$_\alpha$	2.31	2.24	727	2.12	2.70	710	719
10NH–1NH	2.86	4.06	99	3.15	3.31	90	95
10NH–6NH	3.30	5.05	42	3.30	4.36	48	44
6NH–5NH	2.93	3.83	92	3.21	3.18	94	93
5NH–4NH	2.40	3.20	300	4.00	2.46	222	260

We describe in the following the two minimum-Q pairs P_1 and P_2. Their structural parameters and J-coupling constants are collected in Tables VII and VIII, and their structures are shown stereographically in Figure 7.

syn-Correlated Flipping Pair P_1 (E116, G129). The equilibrium represented by these two conformations involves simultaneous dihedral angle changes at ϕ_5 and ϕ_{10} from (+67°, +71°) to (−79°, −58°), respectively. The optimized populations for the two structures are $p_1 = 0.49$ and $p_2 = 0.51$. The mismatch parameter, $Q = 0.21$, is the lowest one found. Both structures contain two *trans*-annular hydrogen bonds, [4]Ala NH·[1]Val CO and [9]Phe NH·[6]Phe CO, that are not affected by the conformational dynamics. They contain another mutually exclusive pair of hydrogen bonds: in the E116

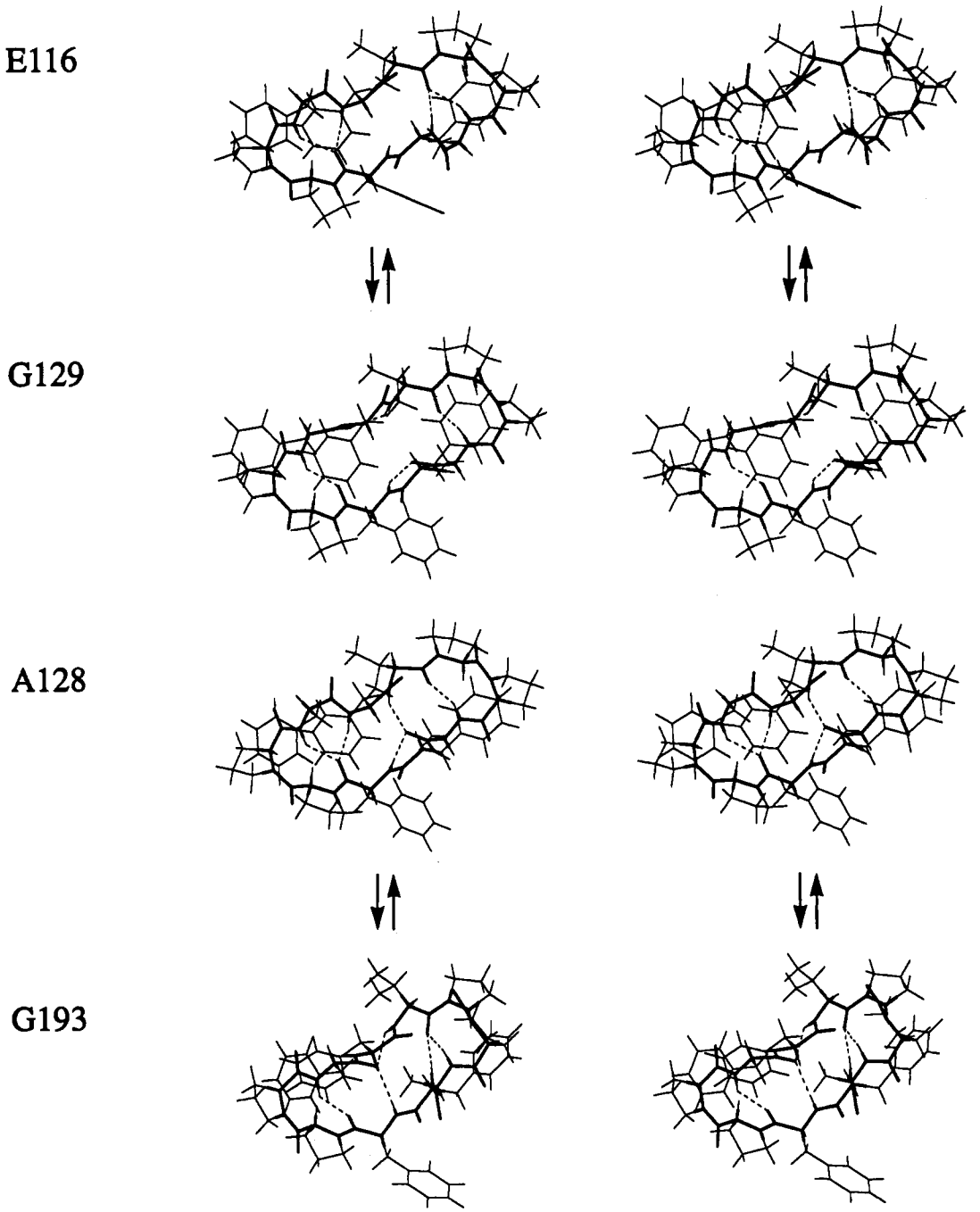

FIGURE 7: Stereographic pictures of the *syn*-pair P_1 = (E116, G129) and the *anti*-pair P_2 = (A128, G193).

conformation the bonds ^{5}Phe NH·^{1}Val CO and ^{10}Phe NH·^{6}Phe CO and in the G129 conformation the bonds ^{1}Val NH·^{9}Phe CO and ^{6}Phe NH·^{4}Ala CO. The dynamics of the two latter hydrogen bonds is responsible for the observed $T_{1\rho}$ effects. The dynamics of the two former hydrogen bonds, involving ^{5}Phe NH and ^{10}Phe NH, seem not to significantly affect the NH chemical shifts and are thus not detectable in the $T_{1\rho}$ experiment. The static hydrogen bonds involving ^{4}Ala NH and ^{9}Phe NH occur almost invariably in the structures shown in Figure 6. They appear to be important for the rigidity of the peptide ring of antamanide.

anti-Correlated Flipping Pair P_2 (A128, G193): This pair with $Q = 0.24$ provides a slightly worse fit of the experimental data than the *syn*-correlated flipping pair. The ϕ_5 and ϕ_{10} angles change here from (−87, 72) to (53, −53). The hydrogen-bonding networks of the two structures can be transformed into each other by a 180° rotation. The two $T_{1\rho}$-relevant hydrogen bonds, ^{1}Val NH·^{9}Phe CO and ^{6}Phe NH·^{4}Ala CO, are opened and closed in an *anti*-correlated manner. Of the four *trans*-annular bonds, the same two as in the pair P_1 remain unaffected while the other two are rearranged, leading to the *anti*-symmetry of the pair. The two conformations are almost equally populated with $p_1 = 0.54$ and $p_2 = 0.46$.

It is revealing to investigate the backbone angular changes in the conversion of the *syn*- and the *anti*-pairs. Figure 8 illustrates the changes in the backbone dihedral angles ϕ_i and ψ_i, i = 1–10, along the peptide ring. It is apparent that the changes are rather local between residues 4–6 and residues 9–1. For the *syn*-pair the changes are in-phase; for the anti-pair, in *anti*-phase. The angular changes for *syn*- and *anti*-pairs are of almost equal amplitude. For the intermediate residues 2–4 and 6–9, there is comparatively little change.

It is tempting to conclude that the conformational changes near residues 5 and 10 are virtually uncorrelated and that they can also proceed independently. Indeed, the conversion from conformation E116 to G129 could proceed in two steps

FIGURE 8: Differences in the backbone dihedral angles ϕ_i and ψ_i within the *syn*- and the *anti*-pair plotted against the residue number i = 1–10, with $\Delta\phi_i = \phi_i^{(1)} - \phi_i^{(2)}$, $\Delta\psi_i = \psi_i^{(1)} - \psi_i^{(2)}$.

with at first one hydrogen bond being formed, e.g., ^{6}Phe NH·^{4}Ala CO, followed in a second step by the formation of the second hydrogen bond. This process is formally equivalent to the pathway E116 ⇌ A128 ⇌ G129 (see Figure 6). Similarly, the pathway E116 ⇌ G193 ⇌ G129 is equally conceivable. On the basis of the presented analysis, such a two-step process cannot be excluded. It amounts to establishing an equilibrium among all four states E116, G129, A128, and G193. An extensive set of linear combinations of these four states was investigated regarding their mismatch parameter values, Q. Invariably, it was found that the smallest Q values were found for the populations $p(-+) = p(+-) = 0$, leading back to the pure *syn*-pair. An admixture of the *anti*-pair did not improve the fit. It should, however, be mentioned that the differences in the Q values are well within the experimental error. It can therefore not be excluded that an admixture of the *anti*-pair to the *syn*-pair indeed exists and that the above four-state equilibrium could correspond to reality.

The possibility of a four-state equilibrium has, in fact, already been mentioned by Kessler et al. (1988). In this reference, an equilibrium between two conformations of antamanide was proposed, the X-ray structure (Karle et al., 1979), which is a (+ +) structure, and a molecular-dynamics-derived structure with a (– –) character. On the basis of the experimental data presented in this paper, these two conformations have individual mismatch values of Q = 0.96 and 1.02, respectively. Their combination in a dynamic system leads to a minimum of Q = 0.39 for a population ratio of 0.55/0.45. The fit is thus significantly worse than for the *syn*- and *anti*-pairs found in this paper. In addition, this combination leads to some large deviations of the average distances, $r_{k,l}^{av}$, from the measured distances, $r_{k,l}^{exp}$: for ^{1}Val NH–^{5}Phe H_α, r^{av} = 2.5 Å and r^{exp} = 3.3 Å; for ^{5}Phe NH–^{4}Ala NH, r^{av} = 2.4 Å and r^{exp} = 3.0 Å; for ^{1}Val NH–^{10}Phe H_α, r^{av} = 2.4 Å and r^{exp} = 3.0 Å; and for ^{10}Phe NH–^{6}Phe NH, r^{av} = 4.5 Å and r^{exp} = 3.1 Å.

On the basis of ultrasonic absorption measurements, Burgermeister et al. (1974) suggested the presence of fast dynamics in antamanide on a time scale between 10^{-6} and 10^{-8} s. In particular, a characteristic "backbone" mode in the range of 10^{-6} s was identified in dioxane and in dioxane/methanol mixtures. In order to determine whether the effects observed in chloroform solution are related to the ultrasonic measurements in dioxane, we have repeated rotating frame relaxation measurements in deuterated dioxane. In this investigation, no rf field dependence of $T_{1\rho}$ was detected over the accessible temperature range from 288 to 310 K (dioxane freezes at 278 K). This observation suggests that the antamanide backbone dynamics is markedly solvent-dependent, and a comparison of measurements in different solvents requires caution. It is evident from eq 2 that a $T_{1\rho}$ measurement samples motional processes in a relatively narrow time window only. It is sensitive to rate constants comparable, within 1 or 2 orders of magnitude, with the applied rf field strength ω_1 (Kopple et al., 1988). Obviously, very rapid motions, that might be present in dioxane solution, are not detected in rotating frame measurements.

CONCLUSIONS

The $T_{1\rho}$ measurement and the conformational search procedure provide evidence for rapid hydrogen bond exchange dynamics at ^{1}Val NH and ^{6}Phe NH of antamanide. Local backbone dihedral angle changes accompany these processes. Two of the most likely pairs of dynamic exchange systems have been identified, designated as the *syn*-pair and the *anti*-pair on the basis of the *syn*-correlated and *anti*-correlated structural changes at the two mentioned residues.

Although the two preferred exchange systems which emerged from the analysis lead to the best fit of the available experimental data, further pair structures cannot yet be excluded from occurring in antamanide. It is also conceivable that a four-state dynamic equilibrium could exist, combining the *syn*- and the *anti*-pair, or that further states of low population take part in the dynamic process. Additional measurements, including ^{15}N and ^{13}C spectroscopy and rotating frame relaxation studies, would be necessary to characterize the ensemble of possible structures in more detail.

In this work, only the peptide backbone conformation is considered, disregarding all side chains and their NOE distance constraints, to limit the number of conformational states to be taken into account. An extension of the MEDUSA procedure to account for all conceivable side-chain motions would require considerably more computer power as the number of conformations to be considered rapidly increases. It should be noted that already the computation of a single antamanide structure for the conformational ensemble requires 30 min of computation time on a Silicon Graphics 4D220. This sets limits on more ambitious applications.

The main result of this work is a new systematic approach to the investigation of dynamic exchange in molecules with internal degrees of freedom. It starts with the computation of a large ensemble of feasible conformations, that may take part in exchange systems, and successively narrows down the ensemble of solutions by applying all available constraints. This approach avoids some of the pitfalls of the reverse procedure where a simple model system is extended and modified whenever it conflicts with additional experimental data. The general nature of the algorithm suggests its usefulness for the investigation of rapid conformational equilibria in medium-size biopolymers.

The MEDUSA procedure, exemplified in this paper, is not the only feasible approach for analyzing molecules with internal degrees of freedom. Fast intramolecular motion can also be directly computed in time by molecular dynamics simulation using classical force fields (Brunne et al., 1993; Schmidt et al., 1993). The quantities observed experimentally can then be computed by a time average over the molecular dynamics trajectory (Brüschweiler et al., 1992) and compared with the experimental results to iteratively improve the parameters of the model system. Whenever the relevant time scale extends to nanoseconds or longer, speed-up procedures overcoming high-potential energy barriers are indispensible for a course-grain sampling in the time domain.

The connection to the real-time behavior is thereby lost. A promising example of such an approach is the procedure recently proposed by Torda et al. (1989, 1990) where a penalty function is introduced that considers time-averaged distance constraints. This procedure improves the search properties of restrained molecular dynamics simulations. Another possibility is the artificial extension of molecular dynamics to a virtual four-dimensional space (W. F. van Gunsteren, private communication).

ACKNOWLEDGMENT

The authors are grateful to Prof. H. Kessler (Technische Universität München) and to Dr. H. Kogler (Hoechst AG) for providing samples of antamanide. Thanks are due to Prof. S. Aimoto (Osaka University) and Prof. M. Kainosho (Tokyo Metropolitan University) for providing a sample of ^{13}C-labeled antamanide. Professor M. Karplus (Harvard University) is thanked for a prerelease of CHARMM-22.

REFERENCES

Abragam, A. (1961) *Principles of Nuclear Magnetism*, Clarendon Press, Oxford.
Bax, A., & Freeman, R. (1982) *J. Am. Chem. Soc. 104*, 1099–1100.
Bax, A., & Davis, D. G. (1985) *J. Magn. Reson. 65*, 355–360.
Bax, A., & Summers, M. F. (1986) *J. Am. Chem. Soc. 108*, 2093–2094.
Bleich, H. E., & Glasel, J. A. (1978) *Biopolymers 17*, 2445–2457.
Bothner-By, A. A., Stephens, R. L., Lee, J., Warren, C. D., & Jeanloz, R. W. (1984) *J. Am. Chem. Soc. 106*, 811–813.
Braun, W., & Gō, N. (1985) *J. Mol. Biol. 186*, 611–626.
Braunschweiler, L., & Ernst, R. R. (1983) *J. Magn. Reson. 53*, 521–528.
Brooks, B. R., Bruccoleri, R. E., Olafsen, B. D., States, D. J., Swaminathan, S., & Karplus, M. (1983) *J. Comput. Chem. 4*, 187–217.
Brunne, R. M., van Gunsteren, W. F., Brüschweiler, R., & Ernst, R. R. (1993) *J. Am. Chem. Soc. 115*, 4764–4768.
Brüschweiler, R., Blackledge, M., & Ernst, R. R. (1991) *J. Biomol. NMR 1*, 3–11.
Brüschweiler, R., Roux, B., Blackledge, M., Griesinger, C., Karplus, M., & Ernst, R. R. (1992) *J. Am. Chem. Soc. 114*, 2289–2302.
Burgermeister, W., Wieland, T., & Winkler, R. (1974) *Eur. J. Biochem. 44*, 311–316.
Bystrov, V. F. (1976) *Prog. Nucl. Magn. Reson. Spectrosc. 10*, 41–82.
Clore, G. M., Brünger, A. T., Karplus, M., & Gronenborn, A. M. (1985) *J. Mol. Biol. 191*, 523–551.
Crippen, G. M. (1981) *Distance Geometry and Conformational Calculations*, Research Studies Press, Chichester.
Crippen, G. M., & Havel, T. F. (1988) *Distance Geometry and Molecular Conformation*, John Wiley & Sons, New York.
Deverell, C., Morgan, R. E., & Strange, J. H. (1970) *Mol. Phys. 18*, 553–559.
de Vlieg, J., Boelens, R., Scheek, R. M., Kaptein, R., & van Gunsteren, W. F. (1986) *Isr. J. Chem. 27*, 181–188.
Ernst, R. R., Bodenhausen, G., & Wokaun, A. (1987) *Principles of NMR in One and Two Dimensions*, Clarendon Press, Oxford.
Faulstich, H., Wieland, T., Walli, A., & Birkmann, K. (1974) *Hoppe-Seyler's Z. Physiol. Chem. 355*, 1162–1163.
Griesinger, C., Sørensen, O. W., & Ernst, R. R. (1985) *J. Am. Chem. Soc. 107*, 6394–6396.
Griesinger, C., Sørensen, O. W., & Ernst, R. R. (1986) *J. Chem. Phys. 85*, 6837–6852.
Griesinger, C., Sørensen, O. W., & Ernst, R. R. (1987) *J. Magn. Reson. 75*, 474–492.
Havel, T. F., & Wüthrich, K. (1984) *Bull. Math. Biol. 45*, 673–698.
Jeener, J., Meier, B. H., Bachmann, P., & Ernst, R. R. (1979) *J. Chem. Phys. 71*, 4546–4553.
Kaptein, R., Zuiderweg, E. R. P., Scheek, R. M., Boelens, R., & van Gunsteren, W. F. (1985) *J. Mol. Biol. 182*, 179–182.
Karle, I. L., Wieland, T., Schermer, D., & Ottenheym, H. C. J. (1979) *Proc. Natl. Acad. Sci. U.S.A. 76*, 1532–1536.
Karpen, M. E., de Haseth, P. L., & Neet, K. E. (1989) *Proteins 6*, 155–167.
Karplus, M. (1959) *J. Chem. Phys. 30*, 11–15.
Karplus, M. (1963) *J. Am. Chem. Soc. 85*, 2870–2871.
Kessler, H., Griesinger, C., Zarbock, J., & Loosli, H. R. (1984) *J. Magn. Reson. 57*, 331–336.
Kessler, H., Griesinger, C., Lautz, J., Müller, A., van Gunsteren, W. F., & Berendsen, H. J. C. (1988) *J. Am. Chem. Soc. 110*, 3393–3396.
Kessler, H., Müller, A., & Pook, K.-H. (1989a) *Liebigs Ann. Chem.* 903–912.
Kessler, H., Bats, J. W., Lautz, J., & Müller, A. (1989b) *Liebigs Ann. Chem.* 913–928.
Kim, Y., & Prestegard, J. H. (1989) *Biochemistry 28*, 8792–8797.

Kline, A. D., Braun, W., & Wüthrich, K. (1988) *J. Mol. Biol. 204*, 675–724.

Kopple, K. D., Bhandary, K. K., Khartha, G., Wang, Y.-S., & Parameswaran, K. N. (1986) *J. Am. Chem. Soc. 108*, 4637–4642.

Kopple, K. D., Wang, Y.-S., Chen, A. G., & Bhandary, K. K. (1988) *J. Am. Chem. Soc. 110*, 4168–4176.

Kumar, A., Wagner, G., Ernst, R. R., & Wüthrich, K. (1981) *J. Am. Chem. Soc. 103*, 3654–3658.

Mádi, Z. L., Griesinger, C., & Ernst, R. R. (1990) *J. Am. Chem. Soc. 112*, 2908–2914.

Marion, D., & Wüthrich, K. (1983) *Biochem. Biophys. Res. Commun. 113*, 967–974.

McCain, D. C., Ulrich, E. L., & Markley, J. L. (1988) *J. Magn. Reson. 80*, 296–305.

Morris, G. A., & Freeman, R. (1978) *J. Magn. Reson. 29*, 433–462.

Müller, A. (1986) Ph.D. Thesis, University of Frankfurt, Germany.

Neuhaus, D., & Williamson, M. (1989) *The Nuclear Overhauser Effect in Structural and Conformational Analysis*, VCH Publishers, New York.

Noggle, J. H., & Shirmer, R. E. (1971) *The Nuclear Overhauser Effect*, Academic Press, New York.

Patel, D. J. (1973) *Biochemistry 12*, 667–676.

Patt, S. L., & Sykes, B. D. (1972) *J. Chem. Phys. 56*, 3182–3184.

Pepermans, H., Tourwe, D., van Binst, G., Boelens, R., Scheek, R. M., van Gunsteren, W. F., & Kaptein, R. (1988) *Biopolymers 27*, 323–338.

Piantini, U., Sørensen, O. W., & Ernst, R. R. (1982) *J. Am. Chem. Soc. 104*, 6800–6801.

Schmidt, J. M., Brüschweiler, R., Ernst, R. R., Dunbrack, R. L., Joseph, D., & Karplus, M. (1993) *J. Am. Chem. Soc.* (in press).

Titman, J. J., & Keeler, J. (1990) *J. Magn. Reson. 89*, 640–646.

Torda, A. E., Scheek, R. M., & van Gunsteren, W. F. (1989) *Chem. Phys. Lett. 157*, 289–294.

Torda, A. E., Scheek, R. M., & van Gunsteren, W. F. (1990) *J. Mol. Biol. 214*, 223–235.

Wagner, G., Stassinopoulou, C. I., & Wüthrich, K. (1984) *Eur. J. Biochem. 145*, 431–436.

Wieland, T., & Faulstich, H. (1978) *Crit. Rev. Biochem.*, 185–260.

Wu, X. L., Xu, P., & Freeman, R. (1989) *J. Magn. Reson. 83*, 404–410.

Wüthrich, K. (1986) *NMR of Proteins and Nucleic Acids*, Wiley-Interscience, New York.